CHEMISTRY OF MATERIALS
Cite This: Chem. Mater. 2019, 31, 4418−4425
Article
pubs.acs.org/cm

Competing Polar and Antipolar Structures in the Ruddlesden−Popper Layered Perovskite $Li_2SrNb_2O_7$

Ritesh Uppuluri,[†] Hirofumi Akamatsu,[*,‡] Arnab Sen Gupta,[§] Huaiyu Wang,[§] Craig M. Brown,[∥,⊥] Kleyser E. Agueda Lopez,[§] Nasim Alem,[§] Venkatraman Gopalan,[*,§] and Thomas E. Mallouk[*,†]

[†]Departments of Chemistry, Biochemistry and Molecular Biology, and Physics, The Pennsylvania State University, University Park, Pennsylvania 16802, United States

[‡]Department of Applied Chemistry, School of Engineering, Kyushu University, Fukuoka, Fukuoka 812-0053, Japan

[§]Department of Materials Science and Engineering, The Pennsylvania State University, University Park, Pennsylvania 16802, United States

[∥]National Institute of Standards and Technology Center for Neutron Research, Gaithersburg, Maryland 20899, United States

[⊥]Department of Chemical and Biomolecular Engineering, University of Delaware, Newark, Delaware 19716, United States

Supporting Information

ABSTRACT: Over the past few years, several studies have reported the existence of polar phases in n = 2 Ruddlesden−Popper layer perovskites by trilinear coupling of oxygen octahedral rotations (OOR) and polar distortions, a phenomenon termed as hybrid improper ferroelectricity. This phenomenon has opened an avenue to expand the available compositions of ferroelectric and piezoelectric layered oxides. In this study, we report a new polar n = 2 Ruddlesden−Popper layered niobate, $Li_2SrNb_2O_7$, which undergoes a structural transformation to an antipolar phase when cooled to 90 K. This structural transition results from a change in the phase of rotation of the octahedral layers within the perovskite slabs across the interlayers. First-principles calculations predicted that the antipolar *Pnam* phase would compete with the polar $A2_1am$ phase and that both would be energetically lower than the previously assigned centrosymmetric *Amam* phase. This phase transition was experimentally observed by a combination of synchrotron X-ray diffraction, powder neutron diffraction, and electrical and nonlinear optical characterization techniques. The competition between symmetry breaking to yield polar layer perovskites and hybrid improper antiferroelectrics provides new insight into the rational design of antiferroelectric materials that can have applications as electrostatic capacitors for energy storage.

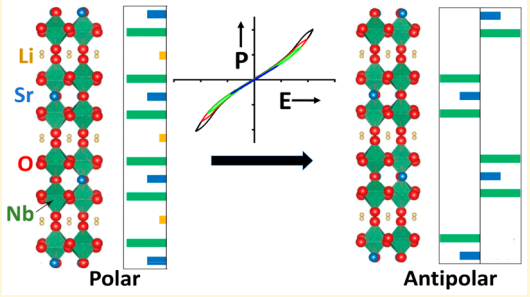

1. INTRODUCTION

Noncentrosymmetric materials are interesting to investigate because of their properties of technological relevance, which include piezoelectrics, ferroelectrics, and multiferroics. Ferroelectric oxides are widely used in ultrasonics, electronics, sensors, capacitors, and actuators and are dominated by ABO_3 perovskites, where polarization is induced by off-centering of $3d^0$ cations by second-order Jahn−Teller (SOJT) active effects.[1] This mechanism limits the range of available compositions of acentric perovskites to those that incorporate $3d^0$ cations that can hybridize with O 2p states.[2] Over the past few years, a series of noncentrosymmetric layered oxides have been predicted by theory and confirmed by experiment, in which inversion symmetry is lifted by a combination of oxygen octahedral rotations (OORs) and *A*-site cation ordering.[3−7] Benedek and Fennie first proposed a "hybrid improper ferroelectricity" (HIF) mechanism,[8] where inversion symmetry is lifted by condensation of two distinct symmetry-breaking modes (rotation and tilting of oxygen octahedra) in the n = 2 Ruddlesden−Popper (RP) compound $Ca_3Mn_2O_7$. This mechanism has since been realized experimentally in several n = 2 RP and Dion-Jacobson (DJ) phase layer perovskites[7,9−17] as well as in perovskite superlattices[18,19] and molecular perovskites.[20] In related work, Rondinelli and co-workers employed group theoretical methods to elucidate the crystal chemical principles that govern the design of acentric n = 1 RP $AA'BO_4$ layer perovskites.[21] Over the past few years, a number of layered oxides with polar space group symmetry have been reported experimentally, and noncentrosymmetricity has been attained by the trilinear coupling of *A*-site cation displacements and OORs.[7,10,22]

More recently, the HIF mechanism has been extended to include antiferroelectric displacements of *A*-site cations driven by a reversal in the direction of OORs. Antiferroelectrics are materials that contain electric dipoles oriented antiparallel within individual domains. They are known to have low

Received: February 25, 2019
Revised: May 29, 2019
Published: June 12, 2019

DOI: 10.1021/acs.chemmater.9b00786
Chem. Mater. 2019, 31, 4418−4425

dielectric loss and are gaining attention as energy storage materials, but they cannot be readily distinguished from other centrosymmetric materials by symmetry.[23] Another limitation is that most known antiferroelectrics are lead-based compounds that are toxic. One approach to overcome these limitations is to search for centrosymmetric materials that have polar metastable phases. Lu et al. predicted a polar-to-nonpolar phase transition in a series of n = 2 RP $A_3B_2O_7$ thin films resulting from compressive and/or axial strain, which could be used to tune weak ferromagnetism in antiferromagnetic compounds by varying the applied electric field at the boundary of the phase transition.[24,25] Similarly, Nowadnick et al. identified the antipolar *Pnam* phase as one of the ferroelectric switching pathways in the n = 2 RP $Ca_3Ti_2O_7$ using group theory, where the polar and antipolar phases differ merely in the octahedral rotation sense ($a^0a^0b^+$) across the interlayers.[26] Recently, Yoshida et al. observed a structural transformation from a polar $A2_1am$ phase to a nonpolar *Pnab* phase by an in-phase to out-of-phase change in the OOR sense in n = 2 RP $Sr_3Zr_2O_7$.[11] This kind of polar-to-antipolar phase transition could be very interesting for realizing new antiferroelectric materials for energy storage applications.

In this study, we report another polar-to-antipolar phase transition in a polycrystalline n = 2 RP phase layered niobate $Li_2SrNb_2O_7$, which contains intergrowths of two perovskite $SrNb_2O_6$ layers with Li−O interlayers when cooled from room temperature to 90 K. The structure of $Li_2SrNb_2O_7$ was previously assigned to the centrosymmetric *Amam* space group,[27] but this study reveals that the polar $A2_1am$ and antipolar *Pnam* structures are energetically more stable by both theory and experiment. The two structures result from the coupling of two octahedral rotations and tilts (denoted by irreducible representations (irreps) X_3^- and X_2^+) along different crystallographic axes and differ merely in the phase of their rotation across the interlayers, i.e., order parameter directions of the irreps. In contrast to studies on $A_3B_2O_7$ systems that mentioned that the nonpolar *Pbcn* phase ($a^-a^-c^-$) competes with the polar $A2_1am$ phase, this study reveals that there is a competition between the polar $A2_1am$ and the antipolar *Pnam* phases, both of which have OORs denoted by $a^-a^-c^+$. In the former structure, the combination of the $X_3^-(a, -a)X_3^-(a, -a)$ and $X_2^+(a, -a)X_2^+(a, -a)$ distortion modes lifts inversion symmetry and induces a polar $\Gamma_5^-(a, a)$ distortion mode, while in the latter structure, the combination of the $X_3^-(a, -a)X_3^-(a, -a)$ and the $X_2^+(a, a)X_2^+(a, -a)$ distortion modes keeps inversion symmetry and induces an antipolar $M_5^-(a, 0)$ distortion mode. A phase diagram of $Li_2SrNb_2O_7$ was determined by combining optical second harmonic generation, temperature-dependent synchrotron X-ray and neutron diffraction, and electrical characterization.

2. EXPERIMENTAL SECTION

2.1. First Principles Calculations. First-principles calculations based on density functional theory (DFT) were carried out using the projector augmented-wave (PAW) method[29,30] and the GGA-PBEsol functional[31−33] as implemented in the Vienna Ab initio Simulation Package (VASP) code.[34−37] [Certain commercial equipment, instruments, or materials are identified in this document. Such identification does not imply recommendation or endorsement by the National Institute of Standards and Technology nor does it imply that the products identified are necessarily the best available for the purpose.] PAW data sets with radial cutoffs of 1.4 Å, 2.1 Å, 1.5 Å, and 0.8 Å were employed for Li, Sr, Nb, and O, respectively. Li 1s, Sr 4s, 4p, and 5s, Nb 4p, 4d, and 5s, and O 2s and 2p orbitals are treated as valence electrons. A plane-wave cutoff energy of 550 and 700 eV was used when structural optimization and density functional perturbation theory (DFPT) calculations were performed, respectively. Γ-centered k-point mesh sampling of 4 × 4 × 1 was used for the $\sqrt{2}\times\sqrt{2}\times 1$ supercells of the conventional $I4/mmm$ unit cell with 24 atoms, except for the DFPT calculations, where an 8 × 8 × 2 mesh was used for the accuracy. Lattice constants and internal atomic coordinates were optimized until residual forces and stresses become less than 0.01 eV/Å and 0.08 GPa, respectively. The Born effective charge tensors were calculated by using DFPT calculations implemented in the VASP code.

Phonon frequencies were derived from the calculated force constants using the PHONOPY code.[38] The phonon dispersion curves were displayed for a standard primitive cell[39,40] along a q-space path based on crystallography.[41] Ground-state structures for $Li_2SrNb_2O_7$ were explored via a method described by Togo and Tanaka[42] as follows: zone-center phonon frequencies were calculated for the $\sqrt{2}\times\sqrt{2}\times 1$ supercell of the conventional cell of the aristotype $I4/mmm$ phase. After perturbing the structure according to the eigenvectors of the obtained imaginary-frequency unstable phonon modes, structure optimizations were performed under symmetry constraints to obtain new stable structures with lower symmetry. Subsequently, we calculated phonon frequencies for the fully relaxed structures to see if unstable modes were still found. If not found, the structure was proven to be dynamically stable. If found, structural perturbations and subsequent optimization were done. This process was repeated until no unstable phonon modes were observed. The cell size was fixed during the structure exploration. We note that zone-boundary phonon modes at the X and M points, which are (1/2 1/2 0) and (0 0 1) in the conventional basis ((0, 0, 1/2) and (1/2, 1/2, −1/2) in the primitive basis),[43] respectively, are folded into the Γ point for the $\sqrt{2}\times\sqrt{2}\times 1$ supercell. Therefore, we explored stable structures within a subspace spanned with linear combinations of atomic displacement modes at the Γ, X, and M points. This method has been applied to ground-state structure explorations for other layer perovskite systems, resulting in a good agreement with the results of experimental structural identifications.[13,14] Symmetry mode analysis was performed to decompose distortions into symmetry-allowed modes with relevant irreps using the AMPLIMODES tool.[44,45]

2.2. Synthesis. Polycrystalline $Li_2SrNb_2O_7$ was synthesized by grinding the precursors Li_2CO_3 (>99%, Aldrich), $SrCO_3$ (>99.9%, Aldrich), and Nb_2O_5 (>99.5%, Alfa Aesar) and heating them at 600 °C for 12 h followed by regrinding, pelletizing, and heating the pellet at 1050 °C for 6 h. The second heating step was repeated until the phase-pure compound was obtained.

2.3. Materials Characterization. Phase purity was confirmed by laboratory X-ray diffraction using a Malvern Panalytical theta−theta X-ray diffractometer (monochromatized Cu Kα radiation). Temperature-dependent synchrotron X-ray diffraction patterns (SXRD) were obtained at the 11-BM-B beamline of Argonne National Laboratory (λ = 0.412632 Å) using 12 Si (111) crystal analyzers and $LaCl_3$ scintillation detectors. Neutron powder diffraction (NPD) was performed at the BT-1 powder diffractometer at NIST using Ge(311) and Ge(733) monochromators with wavelengths of 2.079 and 1.197 Å, respectively. Measurements were performed at 90 and 300 K after loading the sample in a vanadium can. Rietveld refinement of synchrotron X-ray and neutron diffraction patterns were performed by using GSAS-EXPGUI programs.[46,47] Temperature-dependent optical SHG measurements were performed in reflection geometry using a Ti-sapphire laser of incident wavelength 800 ± 20 nm and 80 fs pulses at a frequency of 2 kHz. Polarization-field hysteresis and current versus field measurements were performed by first depositing 200 nm Pt electrodes on a dense pellet for electrical contact and then applying a DC field of 1 kV−10 kV using a Sawyer−Tower circuit at a measurement frequency of 10 Hz. Low temperature dielectric measurements were obtained using a Precision LCR Meter (HP4284A, Agilent Technologies, Santa Clara, CA) at a frequency range of 10^3−10^6 Hz from 300 K down to 100 at 10 K intervals.

DOI: 10.1021/acs.chemmater.9b00786
Chem. Mater. 2019, 31, 4418−4425

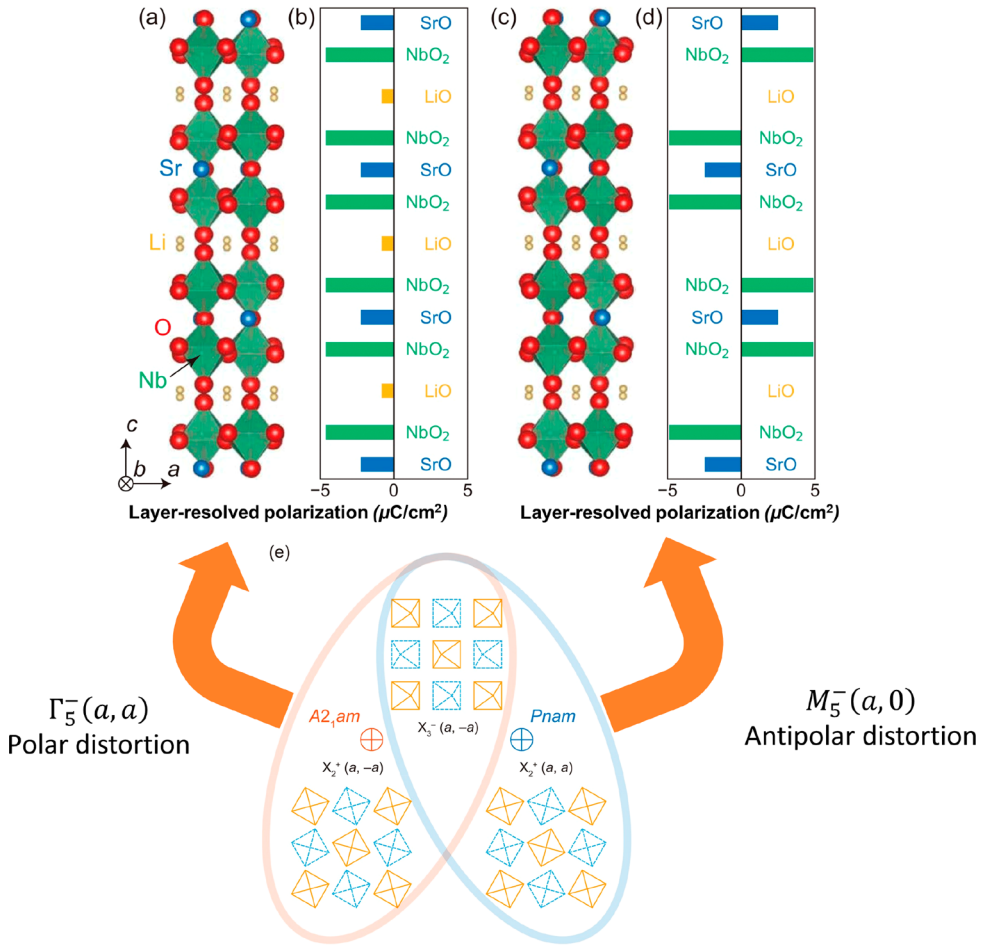

Figure 1. (a) Calculated crystal structure and (b) layer resolved polarization of n = 2 RP $Li_2SrNb_2O_7$ in the polar $A2_1am$ space group. (c) Calculated crystal structure and (d) layer resolved polarization of n = 2 RP $Li_2SrNb_2O_7$ in the antipolar $Pnam$ space group. (e) Schematic of octahedral rotation patterns from which the $A2_1am$ and $Pnam$ structures are constructed with fixed tilt. The blue and orange octahedra represent alternating layers and are corner-shared but their connectivity is omitted to clearly show the rotation patterns.[28]

3. RESULTS AND DISCUSSION

3.1. First Principles Calculations. To check dynamical stability, phonon dispersion curves were calculated for the aristotype $I4/mmm$ phase (Figure S1). Phonon dispersion curves showed structural instabilities at the Γ, X, and M points that were frequently observed to generate lower symmetry structures in other RP systems.[13,14] To thoroughly search for the most stable structural phase by unstable phonon modes based on the calculations, a "family-tree" diagram was constructed that lists the total energies of all the structures with respect to the parent $I4/mmm$ structure (Figure S2).

Table 1. Calculated Energies of $Li_2SrNb_2O_7$ with Different Oxygen Octahedral Rotations (in meV/formula unit)

space group	OOR pattern[a]	total energy[b] (meV/f.u.)	comments
$Amam$	$(\phi\phi 0)$	−81	previously reported[27]
$A2_1am$	$(\phi\phi\psi_z)$	−89	polar structure
$Pnam$	$(\phi\phi\psi_z)(\phi\phi\overline{\Psi}_z)$	−90	antipolar structure
$Cmca$	$(00\psi_z)$	0	

[a]Octahedral rotation patterns are in Aleksandrov notation. [b]Total energies are with respect to the parent $I4/mmm$ structure.

First-principles calculations by DFT revealed that, among the several metastable phases, the polar $A2_1am$ phase was energetically similar to the antipolar $Pnam$ phase and both had the lowest energy with respect to the parent $I4/mmm$ phase (Figure S2). The two most stable structures of $Li_2SrNb_2O_7$ are the antipolar $Pnam$ structure whose net polarizations in alternating double perovskite layers are canceled and the polar $A2_1am$ structure which has net polarization (Figure 1). One of the common maximum supergroups of the two phases is the $Amam$ space group. The corresponding $Amam$ structure has an $a^-a^-c^0$ OOR pattern. Symmetry mode analysis for the two structures with respect to the $Amam$ phase revealed that the polar $A2_1am$ and $Pnam$ phases are derived by $\Gamma_2^-\Gamma_2^-$ and $Y_2^-Y_2^-$ distortion modes from the $Amam$ phase, respectively. Symmetry mode analysis with respect to the parent $I4/mmm$ structure provides us with more insight into the symmetry aspects of the structural features. Both the structures have the same OORs represented by the irreps, X_2^- and X_3^+ (Table S1). The difference is in the direction of the order parameter of the irreps. Depending on the relative direction of the X_2^- and X_3^+ modes, induced modes can be polar (Γ_5^-) or antipolar (M_5^-). In the $A2_1am$ structure, the combination of the $X_2^-(a, -a)$ and $X_3^+(a, -a)$ distortion modes breaks inversion symmetry and induces a polar $\Gamma_5^-(a, a)$ distortion mode. As in hybrid improper ferroelectrics, the

DOI: 10.1021/acs.chemmater.9b00786
Chem. Mater. 2019, 31, 4418−4425

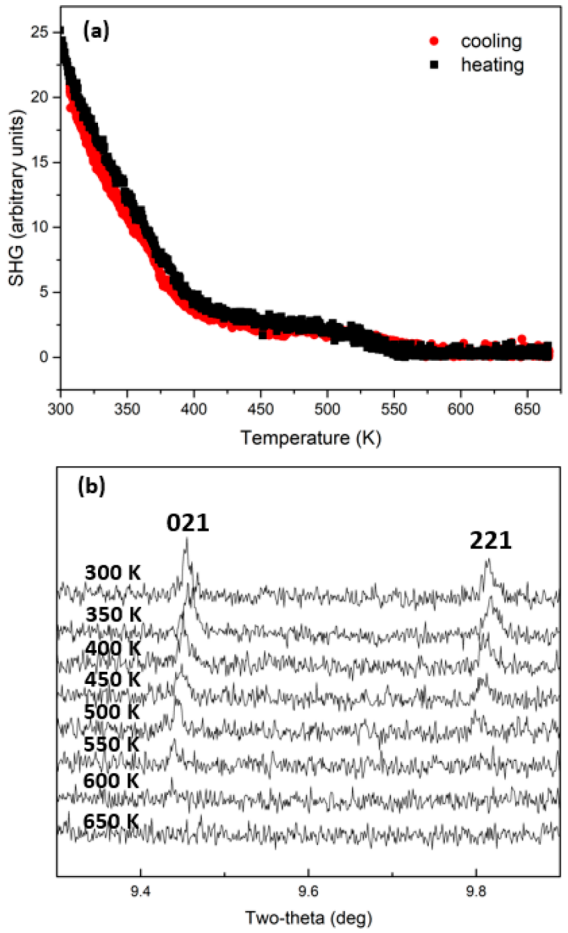

Figure 2. (a) Temperature-dependent SHG measurement of polycrystalline $Li_2SrNb_2O_7$. (b) Tracking the disappearance of the 021 and 221 superlattice reflections with increasing temperature using synchrotron X-ray diffraction.

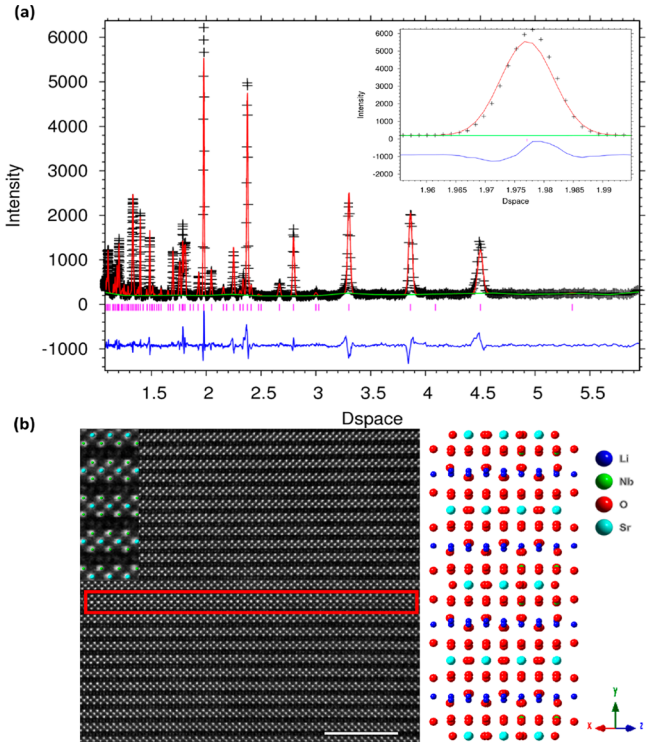

Figure 3. (a) Structural refinement of $Li_2SrNb_2O_7$ neutron diffraction data using the $A2_1am$ model at 300 K ($\chi^2 = 4.51$). The inset shows the enlarged view of the (511) reflection, the profile of which is largely asymmetric. (b) High-angle annular dark-field scanning transmission electron microscopy of $Li_2SrNb_2O_7$ along the [101] zone axis showing a stacking fault highlighted by a red box. The inset shows the mapping of Sr and Nb atoms within the layers that match with the simulated structure on the right. Scale bar is 5 nm.

freezing of two types of OORs drives the polar distortion. On the other hand, in the *Pnam* structure, the combination of the $X_2^-(a, -a)$ and $X_3^+(a, a)$ distortion modes induces an antipolar $M_5^-(a, 0)$ distortion mode, retaining inversion symmetry. The freezing of two types of OORs leads to the antipolar distortion. Thus, the *Pnam* phase could be a hybrid improper antiferroelectric.[13,24] When the directions of tilts are fixed and rotations are varied (Figure 1 e), the two structures have the same rotation direction for the two layers within a perovskite block, but the direction is in-phase across neighboring double perovskite layers. The condensation of the $X_3^-(a, -a)X_3^-(a, -a)$ distortion mode leads to the common supergroup *Amam* phase. The $\Gamma_2^-\Gamma_2^-$ and $Y_2^-Y_2^-$ distortion modes with respect to the *Amam* phase mainly consist of the combination of the $X_2^+(a, -a)X_2^+(a, -a)$ and $\Gamma_5^-(a, a)\Gamma_5^-(a, a)$ distortions and that of the $X_2^+(a, a)X_2^+(a, a)$ and $M_5^-(a, 0)M_5^-(a, 0)$ distortions, respectively (Figure S3). The difference in the rotation patterns for $A2_1am$ and *Pnam* structures can be represented by the Glazer notation $a^-a^-c^+/a^-a^-c^+$ and $a^-a^-c^+/a^-a^-(c^+)$ as described before[48] and can be more easily distinguished using Aleksandrov notation (Table 1).

3.2. Structural Characterization. Optical second harmonic generation (SHG) showed a finite signal at 300 K, consistent with the polar $A2_1am$ structure. The gradual disappearance of the SHG signal at 550 K indicates a transition to a centrosymmetric structure, which was found to be reversible upon cooling (Figure 2a). At low temperatures, SHG shows a thermal hysteresis behavior where the signal peaks at 150 K but does not recover until 200 K during the heating cycle, thus indicating a first-order phase transition (Figure S4). Room temperature synchrotron X-ray diffraction patterns revealed the presence of two weak (021) and (221) superlattice reflections (i.e., $\frac{1}{2}\ \frac{3}{2}\ 0$ and $\frac{1}{2}\ \frac{3}{2}\ 2$ with respect to the $I4/mmm$ structure) that correspond to $\sqrt{2}a_p \times \sqrt{2}a_p \times c_p$ enlargement of the unit cell with respect to the aristotype tetragonal $I4/mmm$ structure (Figure 2b). The room temperature scan matched well with both the $A2_1am$ and the *Amam* structures, but they could not be readily distinguished using X-rays (Figure S5). On the other hand, powder neutron diffraction at 300 K indicated that the room temperature phase could be fitted to the polar $A2_1am$ structure (Figure 3a), which gave a slightly better fit than the *Amam* structure (Figure S6). Thus, the structure was found to be polar at room temperature, in good agreement with the SHG result. The refinement of both synchrotron X-ray and neutron diffraction data was complicated by the presence of stacking faults, which cause largely asymmetric peak profiles (the inset of Figure 3a). The stacking fault could also be imaged by high angle annular dark field scanning transmission electron microscopy (HAADF-STEM) imaging along [101] axis which showed a triple layered perovskite block as highlighted (Figure 3b). Both HRTEM and HAADF-STEM images indicated multiple kinds of stacking faults but did not accurately reveal all the different types of stacking faults present (Figure S7). Tables 2 and 3 list

DOI: 10.1021/acs.chemmater.9b00786
Chem. Mater. 2019, 31, 4418−4425

Table 2. Refined Atomic Positions and Thermal Parameters for $Li_2SrNb_2O_7$ against the $A2_1am$ Model Using SXRD Data at 300 K[a]

atom	Wyckoff position	x	y	z	U_{iso}
Li1	8b	−0.5100(0)	−0.0038(3)	0.7598(6)	0.0000(5)
Nb1	8b	−0.7239(0)	0.2485(2)	0.3845(6)	0.0006(0)
O1	8b	−0.4855(7)	0.0043(1)	0.5959(6)	0.0037(3)
O2	8b	0.0155(6)	0.4934(7)	0.3835(7)	0.0054(0)
O3	8b	−0.7354(8)	0.2202(2)	0.2823(7)	0.0045(0)
O4	4a	−0.7412(5)	0.7874(1)	0.00000	0.0055(5)
Sr1	4a	−0.7369(9)	0.2452(6)	0.00000	0.0046(9)

[a]Values in parentheses indicate one standard deviation. Lattice parameters: a = 5.5918(5) Å, b = 5.5987(0) Å, and c = 18.0102(6) Å and R_{wp} = 31.88% and R_p = 7.75%.

Table 3. Refined Atomic Positions and Thermal Parameters for $Li_2SrNb_2O_7$ against the $A2_1am$ Model Using NPD Data at 300 K[a]

atom	Wyckoff position	x	y	z	U_{iso}
Li1	8b	−0.4659(9)	0.0259(9)	0.7615(9)	−0.0171(9)
Nb1	8b	−0.7385(2)	0.2462(2)	0.3844(9)	0.0046(9)
O1	8b	−0.4950(2)	0.0032(3)	0.5981(5)	0.0002(8)
O2	8b	0.0224(3)	0.5030(8)	0.3838(9)	0.0064(5)
O3	8b	−0.7673(8)	0.2235(1)	0.2810(9)	0.0052(4)
O4	4a	−0.7725(8)	0.7789(1)	0.00000	0.0058(0)
Sr1	4a	−0.7606(2)	0.2562(2)	0.00000	0.0050(1)

[a]Values in parentheses indicate one standard deviation. Lattice parameters: a = 5.5932(0) Å, b = 5.5910(8) Å, and c = 18.0001(9) Å and R_{wp} = 10.08% and R_p = 7.84%.

the refined atomic coordinates for $Li_2SrNb_2O_7$ using SXRD and NPD data, respectively. The refined structure for the $A2_1am$ phase showed a small structural distortion as indicated by small OOR (Figure S8).

At high temperatures, SXRD showed the disappearance of the (021) and (221) superlattice reflections at 650 K and revealed a phase transition to the tetragonal $I4/mmm$ structure. The disappearance of the (221) reflection at 550 K likely corresponds to a centrosymmetric structure as it correlated well with the disappearance of SHG signal, but the space group could not be determined unambiguously. The disappearance of the (221) reflection did not match the $Amam$ model (that is expected from first principles calculations) as it has the same reflection conditions as $A2_1am$ structure. With decreasing temperature, several new reflections appeared at 200 K that matched well with the antipolar $Pnam$ structure. These include reflections such as (141), (270), (290), (341), (490), (690), and many more that are forbidden in the $A2_1am$ space group, as they do not obey the reflection condition $k + l = 2n$ for A-centered lattices. Figure 4a,b tracks the thermal evolution of the (141) and (341) reflections with temperature and reveals that there is a marked increase in the intensity of these reflections at around 200 K. However, in these temperature ranges, there seems to be a coexistence of both polar and antipolar phases, thus indicating a diffuse phase transition between the $A2_1am$ and the $Pnam$ phases. Powder neutron diffraction collected at 90 K could be fitted with the $Pnam$ model (Figure S9 and Table S2).

To further elucidate the electrical properties of the emergent phase at low temperatures, polarization-field hysteresis loops, $P(E)$, were measured under liquid nitrogen. The $P(E)$ measurements suggested antiferroelectric behavior at 77 K as shown by the double hysteresis loops with polarization values of ≈1.0 $\mu C/cm^2$, although the loops could not be saturated (Figure 4c). The measured polarization was much lower than the calculated value by DFT (25 $\mu C/cm^2$). The low polarization value was attributed to the polycrystalline nature of the sample which had random orientations and was consistent with previous polarization values obtained on polycrystalline samples.[13] Additionally, the current (I) vs voltage (V) curve showed a peak in the current at high electric fields resulting from polarization that is suggestive of antiferroelectric behavior (Figure S10). Room temperature $P(E)$ measurements showed a high loss in capacitance values due to conductivity of lithium ions (Figure S11).

Temperature-dependent dielectric permittivity values were measured in the frequency ranges of 10^3−10^6 Hz in the temperature range of 100−300 K and are plotted as dielectric constant ε' vs T as well as $1/\varepsilon'$ vs T in Figure 5a,b. An increase in the measured relative permittivity values was observed at all frequencies upon decreasing the temperature to 200 K. The dielectric anomaly correlated well with antiferroelectric behavior that emerges starting at 200 K as antiferroelectric materials are known to have large dielectric constants (Figure 5a). A plot of inverse dielectric permittivity vs T ($1/\varepsilon'$ vs T) indicated that it follows the Curie−Weiss law, $\varepsilon' = C/(T - \theta)$ for $T > 206$ K, where C is a Curie constant and θ is a Curie−Weiss temperature. Based on the Curie−Weiss fit, $C = 1.1 \times 10^4$ K and $\theta = -0.33$ K. The extremely low θ value was attributed to a series addition of capacitance values from both polar and nonpolar domains possibly due to the presence of grain boundaries thus making the resulting capacitance values much lower.

3.3. Origin of Ferroelectricity/Antiferroelectricity. The polar-to-antipolar phase transition shown upon cooling down to 90 K is the result of a change in the OOR direction across the interlayers, and the two phases compete, thus resulting in a diffuse phase transition in the SXRD data. In this system, both the SOJT mechanism, where d(Nb)−p(O) charge transfer induces a polarization in the NbO_2 layer, and the trilinear

DOI: 10.1021/acs.chemmater.9b00786
Chem. Mater. 2019, 31, 4418−4425

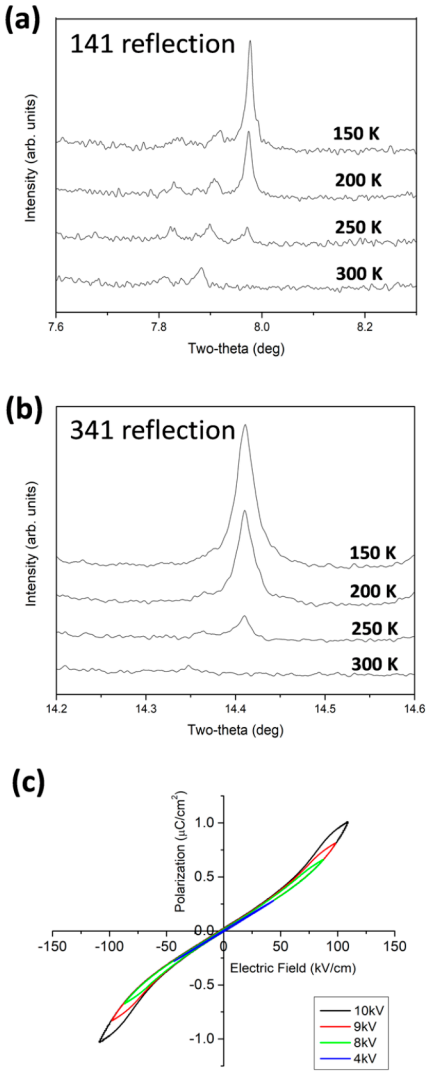

Figure 4. Thermal evolution of (a) (141) reflection and (b) (341) reflection as a function of temperature. (c) Polarization−electric field hysteresis measurement of $Li_2SrNb_2O_7$ at 77 K.

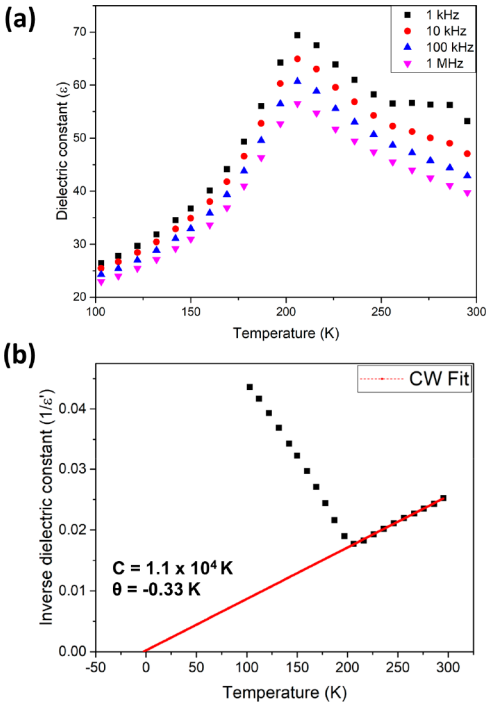

Figure 5. Temperature-dependent dielectric permittivity measurements of $Li_2SrNb_2O_7$ plotted as (a) ε' vs T and (b) inverse dielectric permittivity vs T at 1 MHz.

coupling of OOR and OOT distortions with A-site cation displacement played an important role in stabilizing the polar and antipolar phases. From Figure 1, the calculated layer-resolved polarization values indicated that, for both $A2_1am$ and *Pnam* phases, the polarization in the NbO_2 layers enhances the polarization in the SrO layers. This is in contrast to $Sr_3Zr_2O_7$, where polarization is merely contributed by A-site cation displacements induced by OOR and OOT distortions.[13] Considering each distortion mode individually, calculations revealed that the out-of-phase OOT mode resulted in a net energy gain but the in-phase OOR mode did not result in energy minimization (Figure S12a). This observation is in sharp contrast to previous studies on hybrid improper ferroelectrics, where each of the modes resulted in significant energy gains. Calculations were also performed to determine the energetics of the coupling of OOR and OOT modes with the displacement of A-site cations (Figure S12b,c). Both polar and antipolar phases were found to be energetically most stable when they had a finite amplitude of OOR and OOT modes coupled with A-site displacements. This observation was corroborated with calculations on the energetic contributions of the different distortion modes which revealed that the trilinear coupling of X_2^+ and X_3^- modes with the polar (or antipolar) modes resulted in the lowest energy structure (Figure S13). Hence, the hybrid improper ferroelectricity/antiferroelectricity mechanism plays an equally important role in stabilizing the polar phase for $Li_2SrNb_2O_7$.

4. CONCLUSION

In summary, this study has revealed a new polar layered oxide, $Li_2SrNb_2O_7$, with an $A2_1am$ structure at room temperature that shows a phase transition to an antipolar *Pnam* phase upon cooling to 200 K. On heating to high temperatures, it undergoes a phase transition to an unknown centrosymmetric phase at 550 K and a tetragonal $I4/mmm$ structure at 650 K. Figure 6 shows the phase diagram of $Li_2SrNb_2O_7$ as a function of temperature. Temperature-dependent second harmonic generation revealed a noncentrosymmetric-to-centrosymmetric phase transition upon cooling from room temperature to 90 K. The polar-to-antipolar phase transition was also confirmed by polarization-hysteresis loop measurements which showed double hysteresis behavior at 90 K and an increase in the dielectric susceptibility at 200 K. The phase transition was attributed to a competition between hybrid improper ferroelectric/antiferroelectric mechanisms, where the polar/antipolar phases were stabilized by a trilinear coupling with oxygen octahedral distortions. Additionally, the SOJT mechanism also plays an important role in stabilizing the polar/antipolar phases in this system. The polar-to-antipolar phase transition offers a novel path to realize antiferroelectric materials in compounds that have energetically similar polar and antipolar structural phases. New materials discovered by this method can be interesting for applications in energy storage devices.

DOI: 10.1021/acs.chemmater.9b00786
Chem. Mater. 2019, 31, 4418−4425

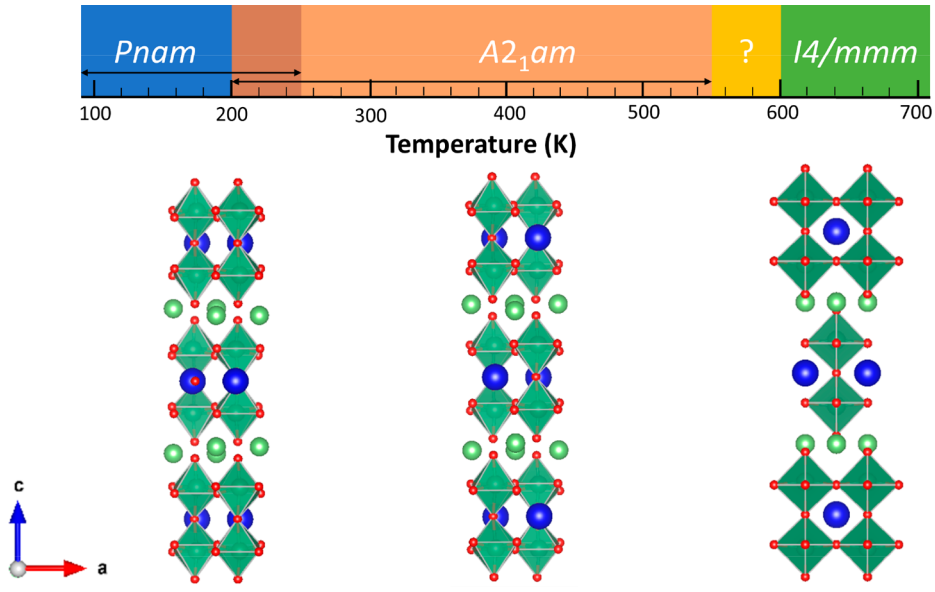

Figure 6. Phase diagram of $Li_2SrNb_2O_7$ as a function of temperature.

■ ASSOCIATED CONTENT

Supporting Information

The Supporting Information is available free of charge on the ACS Publications website at DOI: 10.1021/acs.chemmater.9b00786.

Family tree diagram of all structures from first-principles calculations, energy-band structures of $Li_2SrNb_2O_7$, low temperature SHG measurement, refinements of SXRD and NPD data, TEM images showing stacking faults, additional results from electrical measurements, and results from first-principles calculations (PDF)

■ AUTHOR INFORMATION

ORCID

Arnab Sen Gupta: 0000-0002-0801-6555
Nasim Alem: 0000-0003-0009-349X
Thomas E. Mallouk: 0000-0003-4599-4208

Notes

The authors declare no competing financial interest.

■ ACKNOWLEDGMENTS

We thank Susan Trolier-McKinstry for helpful discussions about the interpretation of the dielectric measurements. This work was supported by the National Science Foundation under MRSEC Grant Number DMR-1420620 and Japan Society for the Promotion of Science (JSPS) KAKENMI Grant No. JP18H01892. This research used resources of the Advanced Photon Source, a U.S. Department of Energy (DOE) Office of Science User Facility operated for the DOE Office of Science by Argonne National Laboratory under Contract No. DE-AC02-06CH11357.

■ REFERENCES

(1) Bersuker, I. B. Pseudo-Jahn–Teller Effect—A Two-State Paradigm in Formation, Deformation, and Transformation of Molecular Systems and Solids. *Chem. Rev.* **2013**, *113*, 1351–1390.

(2) Cohen, R. E. Origin of Ferroelectricity in Perovskite Oxides. *Nature* **1992**, *358*, 136–38.

(3) Akamatsu, H.; Fujita, K.; Kuge, T.; Sen Gupta, A.; Togo, A.; Lei, S.; Xue, F.; Stone, G.; Rondinelli, J. M.; Chen, L.-Q. Inversion Symmetry Breaking by Oxygen Octahedral Rotations in the Ruddlesden-Popper $NaRTiO_4$ Family. *Phys. Rev. Lett.* **2014**, *112*, 187602.

(4) Gupta, A. S.; Akamatsu, H.; Strayer, M. E.; Lei, S.; Kuge, T.; Fujita, K.; dela Cruz, C.; Togo, A.; Tanaka, I.; Tanaka, K. Improper Inversion Symmetry Breaking and Piezoelectricity through Oxygen Octahedral Rotations in Layered Perovskite Family, $LiRTiO_4$ (R = Rare Earths). *Adv. Electron. Mater.* **2016**, *2*, 1500196.

(5) Strayer, M. E.; Gupta, A. S.; Akamatsu, H.; Lei, S.; Benedek, N. A.; Gopalan, V.; Mallouk, T. E. Emergent Noncentrosymmetry and Piezoelectricity Driven by Oxygen Octahedral Rotations in N = 2 Dion–Jacobson Phase Layer Perovskites. *Adv. Funct. Mater.* **2016**, *26*, 1930–1937.

(6) Sen Gupta, A.; Akamatsu, H.; Brown, F. G.; Nguyen, M. A. T.; Strayer, M. E.; Lapidus, S.; Yoshida, S.; Fujita, K.; Tanaka, K.; Tanaka, I. Competing Structural Instabilities in the Ruddlesden–Popper Derivatives $HRTiO_4$ (R = Rare Earths): Oxygen Octahedral Rotations Inducing Noncentrosymmetricity and Layer Sliding Retaining Centrosymmetricity. *Chem. Mater.* **2017**, *29*, 656–665.

(7) Zhu, T.; Cohen, T.; Gibbs, A. S.; Zhang, W.; Halasyamani, P. S.; Hayward, M. A.; Benedek, N. A. Theory and Neutrons Combine To Reveal a Family of Layered Perovskites without Inversion Symmetry. *Chem. Mater.* **2017**, *29*, 9489–9497.

(8) Benedek, N. A.; Fennie, C. J. Hybrid Improper Ferroelectricity: A Mechanism for Controllable Polarization-Magnetization Coupling. *Phys. Rev. Lett.* **2011**, *106*, 107204.

(9) Oh, Y. S.; Luo, X.; Huang, F.-T.; Wang, Y.; Cheong, S.-W. Experimental Demonstration of Hybrid Improper Ferroelectricity and the Presence of Abundant Charged Walls in $(Ca,Sr)_3Ti_2O_7$ Crystals. *Nat. Mater.* **2015**, *14*, 407–13.

(10) Pitcher, M. J.; Mandal, P.; Dyer, M. S.; Alaria, J.; Borisov, P.; Niu, H.; Claridge, J. B.; Rosseinsky, M. J. Tilt Engineering of Spontaneous Polarization and Magnetization above 300 K in a Bulk Layered Perovskite. *Science* **2015**, *347*, 420–424.

(11) Dixon, C. A. L.; McNulty, J. A.; Knight, K. S.; Gibbs, A. S.; Lightfoot, P. Phase Transition Behavior of the Layered Perovskite $CsBi_{0.6}La_{0.4}Nb_2O_7$: A Hybrid Improper Ferroelectric. *Crystals* **2017**, *7*, 135.

(12) Wang, Y.; Huang, F.-T.; Luo, X.; Gao, B.; Cheong, S.-W. The First Room-Temperature Ferroelectric Sn Insulator and Its Polarization Switching Kinetics. *Adv. Mater.* **2017**, *29*, 1601288.

DOI: 10.1021/acs.chemmater.9b00786
Chem. Mater. 2019, 31, 4418–4425

(13) Yoshida, S.; Fujita, K.; Akamatsu, H.; Hernandez, O.; Sen Gupta, A.; Brown, F. G.; Padmanabhan, H.; Gibbs, A. S.; Kuge, T.; Tsuji, R. Ferroelectric $Sr_3Zr_2O_7$: Competition between Hybrid Improper Ferroelectric and Antiferroelectric Mechanisms. *Adv. Funct. Mater.* **2018**, *28*, 1801856.
(14) Yoshida, S.; Akamatsu, H.; Tsuji, R.; Hernandez, O.; Padmanabhan, H.; Sen Gupta, A.; Gibbs, A. S.; Mibu, K.; Murai, S.; Rondinelli, J. M. Hybrid Improper Ferroelectricity in $(Sr,Ca)_3Sn_2O_7$ and Beyond: Universal Relationship between Ferroelectric Transition Temperature and Tolerance Factor in n = 2 Ruddlesden-Popper Phases. *J. Am. Chem. Soc.* **2018**, *140*, 15690−15700.
(15) Zhu, T.; Khalsa, G.; Havas, D. M.; Gibbs, A. S.; Zhang, W.; Halasyamani, P. S.; Benedek, N. A.; Hayward, M. A. Cation Exchange as a Mechanism To Engineer Polarity in Layered Perovskites. *Chem. Mater.* **2018**, *30*, 8915−8924.
(16) Liu, X. Q.; Wu, J. W.; Shi, X. X.; Zhao, H. J.; Zhou, H. Y.; Qiu, R. H.; Zhang, W. Q.; Chen, X. M. Hybrid Improper Ferroelectricity in Ruddlesden-Popper $Ca_3(Ti,Mn)_2O_7$ Ceramics. *Appl. Phys. Lett.* **2015**, *106*, 202903.
(17) Lee, M. H.; Chang, C.-P.; Huang, F.-T.; Guo, G. Y.; Gao, B.; Chen, C. H.; Cheong, S.-W.; Chu, M.-W. Hidden Antipolar Order Parameter and Entangled Neel-Type Charged Domain Walls in Hybrid Improper Ferroelectrics. *Phys. Rev. Lett.* **2017**, *119*, 157601.
(18) Xu, B.; Wang, D.; Zhao, H. J.; Íñiguez, J.; Chen, X. M.; Bellaiche, L. Hybrid Improper Ferroelectricity in Multiferroic Superlattices: Finite-Temperature Properties and Electric-Field-Driven Switching of Polarization and Magnetization. *Adv. Funct. Mater.* **2015**, *25*, 3626−3633.
(19) Young, J.; Moon, E. J.; Mukherjee, D.; Stone, G.; Gopalan, V.; Alem, N.; May, S. J.; Rondinelli, J. M. Polar Oxides without Inversion Symmetry through Vacancy and Chemical Order. *J. Am. Chem. Soc.* **2017**, *139*, 2833−2841.
(20) Boström, H. L. B.; Senn, M. S.; Goodwin, A. L. Recipes for Improper Ferroelectricity in Molecular Perovskites. *Nat. Commun.* **2018**, *9*, 2380.
(21) Balachandran, P. V.; Puggioni, D.; Rondinelli, J. M. Crystal-Chemistry Guidelines for Noncentrosymmetric A_2BO_4 Ruddlesden−Popper Oxides. *Inorg. Chem.* **2014**, *53*, 336−348.
(22) Kim, S. W.; Emge, T. J.; Deng, Z.; Uppuluri, R.; Collins, L.; Lapidus, S. H.; Segre, C. U.; Croft, M.; Jin, C.; Gopalan, V. $YCrWO_6$: Polar and Magnetic Oxide with $CaTa_2O_6$-Related Structure. *Chem. Mater.* **2018**, *30*, 1045−1054.
(23) Yao, Z.; Song, Z.; Hao, H.; Yu, Z.; Cao, M.; Zhang, S.; Lanagan, M. T.; Liu, H. Homogeneous/Inhomogeneous-Structured Dielectrics and Their Energy-Storage Performances. *Adv. Mater.* **2017**, *29*, 1601727.
(24) Lu, X.-Z.; Rondinelli, J. M. Epitaxial-Strain-Induced Polar-to-Nonpolar Transitions in Layered Oxides. *Nat. Mater.* **2016**, *15*, 951.
(25) Lu, X.-Z.; Rondinelli, J. M. Room Temperature Electric-Field Control of Magnetism in Layered Oxides with Cation Order. *Adv. Funct. Mater.* **2017**, *27*, 1604312.
(26) Nowadnick, E. A.; Fennie, C. J. Domains and Ferroelectric Switching Pathways in $Ca_3Ti_2O_7$ from First Principles. *Phys. Rev. B: Condens. Matter Mater. Phys.* **2016**, *94*, 104105.
(27) Floros, N.; Michel, C.; Hervieu, M.; Raveau, B. New n = 2 Members of the $Li_2Sr_{n-1}MO_{3n+1}$ Family, Closely Related to the Ruddlesden-Popper Phases: Structure and Non-Stoichiometry. *J. Mater. Chem.* **1999**, *9*, 3101−3106.
(28) Aleksandrov, K. S. Structural phase transitions in layered perovskite-like crystals. *Crystallographic Reports*; Springer: 1995; Vol. *40*.
(29) Blöchl, P. E. Projector Augmented-Wave Method. *Phys. Rev. B: Condens. Matter Mater. Phys.* **1994**, *50*, 17953−17979.
(30) Kresse, G.; Joubert, D. From Ultrasoft Pseudopotentials to the Projector Augmented-Wave Method. *Phys. Rev. B: Condens. Matter Mater. Phys.* **1999**, *59*, 1758−1775.
(31) Perdew, J. P.; Burke, K.; Ernzerhof, M. Generalized Gradient Approximation Made Simple. *Phys. Rev. Lett.* **1996**, *77*, 3865−3868.
(32) Perdew, J. P.; Burke, K.; Ernzerhof, M. Generalized Gradient Approximation Made Simple. *Phys. Rev. Lett.* **1997**, *78*, 1396.
(33) Perdew, J. P.; Ruzsinszky, A.; Csonka, G. I.; Vydrov, O. A.; Scuseria, G. E.; Constantin, L. A.; Zhou, X.; Burke, K. Restoring the Density-Gradient Expansion for Exchange in Solids and Surfaces. *Phys. Rev. Lett.* **2008**, *100*, 136406.
(34) Kresse, G.; Hafner, J. Ab Initio Molecular Dynamics for Open-Shell Transition Metals. *Phys. Rev. B: Condens. Matter Mater. Phys.* **1993**, *48*, 13115−13118.
(35) Kresse, G.; Hafner, J. Ab Initio Molecular Dynamics for Liquid Metals. *Phys. Rev. B: Condens. Matter Mater. Phys.* **1993**, *47*, 558−561.
(36) Kresse, G.; Furthmüller, J. Efficiency of Ab-Initio Total Energy Calculations for Metals and Semiconductors Using a Plane-Wave Basis Set. *Comput. Mater. Sci.* **1996**, *6*, 15−50.
(37) Kresse, G.; Furthmüller, J. Efficient Iterative Schemes for Ab Initio Total-Energy Calculations Using a Plane-Wave Basis Set. *Phys. Rev. B: Condens. Matter Mater. Phys.* **1996**, *54*, 11169−11186.
(38) Togo, A.; Tanaka, I. First Principles Phonon Calculations in Materials Science. *Scr. Mater.* **2015**, *108*, 1−5.
(39) Hinuma, Y.; Togo, A.; Hayashi, H.; Tanaka, I. Choice of basis vectors for conventional unit cells revisited. 2015, arXiv:cond-mat/1506.01455. arXiv.org e-Print archive. http://arxiv.org/abs/1506.01455 (accessed Nov. 30, 2017).
(40) Setyawan, W.; Curtarolo, S. High-Throughput Electronic Band Structure Calculations: Challenges and Tools. *Comput. Mater. Sci.* **2010**, *49*, 299−312.
(41) Hinuma, Y.; Pizzi, G.; Kumagai, Y.; Oba, F.; Tanaka, I. Band Structure Diagram Paths Based on Crystallography. *Comput. Mater. Sci.* **2017**, *128*, 140−184.
(42) Togo, A.; Tanaka, I. Evolution of Crystal Structures in Metallic Elements. *Phys. Rev. B: Condens. Matter Mater. Phys.* **2013**, *87*, 184104.
(43) Aroyo, M. I.; Orobengoa, D.; de la Flor, G.; Tasci, E. S.; Perez-Mato, J. M.; Wondratschek, H. Brillouin-Zone Database on the Bilbao Crystallographic Server. *Acta Crystallogr., Sect. A: Found. Adv.* **2014**, *70*, 126−137.
(44) Orobengoa, D.; Capillas, C.; Aroyo, M. I.; Perez-Mato, J. M. AMPLIMODES}: Symmetry-Mode Analysis on the Bilbao Crystallographic Server. *J. Appl. Crystallogr.* **2009**, *42*, 820−833.
(45) Perez-Mato, J. M.; Orobengoa, D.; Aroyo, M. I. Mode Crystallography of Distorted Structures. *Acta Crystallogr., Sect. A: Found. Crystallogr.* **2010**, *66*, 558−590.
(46) Larson, A. C.; Von Dreele, R. B. *General Structure Analysis System*; Los Alamos National Laboratory Report LAUR 86-748; Los Alamos National Laboratory: 2000.
(47) Toby, B. H. *EXPGUI*, a graphical user interface for *GSAS*. *J. Appl. Crystallogr.* **2001**, *34*, 210−13.
(48) Zhang, R.; Senn, M. S.; Hayward, M. A. Directed Lifting of Inversion Symmetry in Ruddlesden−Popper Oxide−Fluorides: Toward Ferroelectric and Multiferroic Behavior. *Chem. Mater.* **2016**, *28*, 8399−8406.

DOI: 10.1021/acs.chemmater.9b00786
Chem. Mater. 2019, 31, 4418−4425